Catalysis Science & Technology

ROYAL SOCIETY OF CHEMISTRY

PAPER

View Article Online
View Journal | View Issue

Cite this: *Catal. Sci. Technol.*, 2025, 15, 4528

High-performance Zn(II)-based coordination polymer as an electrode material for pseudocapacitive energy storage and hydrogen evolution†

Samika Anand, [a] Abhishek Kumar,[cd] Kalathiparambil Rajendra Pai Sunajadevi, *[a] Channabasaveshwar V. Yelamaggad *[bcd] and Kaustava Bhattacharyya [ef]

Recently, multifunctional materials for energy storage and production have been investigated to address diverse energy challenges. However, innovative methodologies focusing on the design and synthesis of novel materials remain essential to effectively tackle persistent challenges such as material degradation, high overpotentials, low conductivity, inferior cycling performance, elevated resistance, and high production costs. Working along these lines, we report a simplistic gram-scale synthesis, characterization, and excellent electrochemical behavior of a Zn(II)-based coordination polymer (COP) abbreviated as Zn(DAB). It has been obtained in quantitative yields through a facile one-pot reaction between N_4-ligand, 3,3′-diaminobenzidine (DAB), and Zn(II) ions, derived from $Zn(OAc)_2{\cdot}2H_2O$, at room temperature. The proposed structure of the COP was established through a series of standard spectroscopic and electron microscopic analyses. These methods unveiled the self-assembly of indefinitely long coordination strands, resulting in a two-dimensional (2D) layered structure. Zn(DAB), when probed for its electrochemical characteristics, reveals exemplary results. The material showed a high specific capacitance of 2091.4 F g^{-1}, calculated at 1 A g^{-1} with 92% retention over 5000 charge–discharge cycles. Additionally, the COP also exhibited a subservient overpotential of 263 mV at a current density of 10 mA cm^{-2} for the hydrogen evolution reaction. These results highlight the promising potential of Zn(DAB) as a multifunctional electrode material for sustainable energy applications.

Received 8th March 2025,
Accepted 8th June 2025

DOI: 10.1039/d5cy00282f

rsc.li/catalysis

Introduction

The escalating energy demand worldwide has led to an energy crisis, spurring intensive research efforts towards reliable and cost-effective materials for storing and generating energy, due to the diminishing and unsustainable nature of non-renewable energy sources. Advanced materials capable of storing, transporting, or converting energy have garnered significant attention for both fundamental research and practical applications. In this context, the development of functional materials for energy storage and production has emerged as a pivotal area of research and innovation. In the realm of harvesting and producing energy, particular emphasis has been placed on materials for energy storage devices (supercapacitors) and electrocatalytic water splitting (particularly for hydrogen production).[1,2]

Owing to their appealing characteristics such as long cycling life, rapid charge/discharge rates, high specific capacity/power density, affordability, and eco-friendliness, supercapacitors serve as standalone power sources. Their ease of operability and wide temperature tolerance make them suitable for use under harsh environmental conditions, including automotive, aerospace, and industrial applications. Supercapacitors are categorized into electric double-layer capacitors (EDLCs), pseudocapacitors, and hybrid supercapacitors based on their charge storage mechanisms. EDLCs employ double-layer electrodes for electrostatic charge storage (non-faradaic), pseudocapacitors store charge through faradaic redox reactions between electrodes and electrolytes,

[a] *Department of Chemistry, Christ University, Bangalore-560029, Karnataka, India. E-mail: sunajadevi.kr@christuniversity.in*
[b] *SJB Institute of Technology, Health & Education City, Kengeri, Bengaluru – 560060, Karnataka, India*
[c] *Department of Chemistry, Manipal Institute of Technology, Manipal Academy of Higher Education, Manipal 576104, Karnataka, India*
[d] *Centre for Nano and Soft Matter Sciences (CeNS), Arkavathi, Survey No.7, Shivanapura, Dasanapura Hobli, Bengaluru 562162, Karnataka, India. E-mail: yelamaggad@cens.res.in*
[e] *Chemistry Division, Bhabha Atomic Research Centre, Mumbai, 400085, India*
[f] *Homi Bhabha National Institute, Anushaktinagar, Mumbai, 400094, India*
† Electronic supplementary information (ESI) available. See DOI: https://doi.org/10.1039/d5cy00282f

while hybrid supercapacitors combine both faradaic and non-faradaic processes for charge storage.[3]

On the other hand, electrochemical water splitting represents a key pathway in the production of clean hydrogen. It involves electrolysis of water in an electrochemical cell where the two electrodes facilitate electrochemical reactions that lead to the decomposition of water into its constituent gases.[4] The two half-reactions lead to the production of hydrogen *via* the hydrogen evolution reaction (HER) and oxygen *via* the oxygen evolution reaction (OER). Hydrogen can store energy efficiently, making it useful for buffering intermittent renewable energy sources like wind and solar. It can also be used as a fuel for various forms of transportation, including hydrogen fuel cell vehicles and hydrogen-powered trains, in addition to a wide range of industrial processes, such as refining, ammonia production, and metal processing. The shift from fossil fuels to hydrogen energy can significantly reduce carbon emissions and aid in meeting climate goals.[5,6] Additionally, the concurrent generation of oxygen during water splitting offers valuable uses in medical, metallurgical, and wastewater treatment industries. Transitioning from conventional fossil fuels to hydrogen-based energy systems, with the added advantage of oxygen by-products, can substantially lower carbon emissions and support global climate action initiatives.[7] Continued advancements in water splitting technologies and their integration into energy systems are crucial for a cleaner, more resilient, and sustainable energy future.[8]

Pt and RuO_2/IrO_2 are known to be excellent catalysts for the HER and OER, respectively. Hence, they are often used as a benchmark or standard reference material for comparing the catalytic activity of other materials in electrochemical studies. The overpotential in the context of HER and OER refers to the additional potential (voltage) that must be applied to drive the reaction at a certain rate compared to the thermodynamic potential. The overpotential accounts for the energy losses and kinetic barriers associated with the electrochemical process. Although Pt, RuO_2, and IrO_2 are effective, the high cost and scarcity of these metals have led researchers to develop alternative catalysts with lower overpotentials and improved cost-effectiveness.

In the past few decades, extensive research efforts have been dedicated to the development of various functional materials with enhanced capacitive and electrocatalytic performance. Electrode materials investigated for supercapacitors and electrocatalytic water splitting encompass metal oxide/hydroxide-based composites,[9] metal carbides/nitrides,[10] conducting polymers,[11] carbonaceous materials,[12] and porous materials.[13] Among these, coordination polymers (COPs) have emerged as particularly promising candidates.

Coordination polymers (COPs) are state-of-the-art hybrid materials that have recently been investigated for several applications, particularly energy storage in supercapacitors and electrochemical water splitting. They constitute a class of functional materials characterized by metal nodes (often transition metal ions) forming coordinate bonds with organic ligands, featuring well-ordered and porous structures. The coordination bonds between metal and ligands act as the structural framework, while the organic ligands, including functional groups like carboxylates, pyridines, or imidazoles, serve as connectors between metal nodes, forming one-dimensional (1D) chains.[14–16] These chains can undergo self-assembly, facilitated by secondary interactions such as hydrogen bonding, π–π stacking, dipole–dipole, and van der Waals forces, leading to the formation of 2D sheets or 3D frameworks. The structural diversity of COPs, influenced by the choice of metal ions and ligands, allows for customization to meet specific application requirements.[16,17] COPs have been extensively researched for their expanded surface area, enduring porosity and adsorption capabilities as well as optical and magnetic properties. COPs, particularly those based on transition metals with d^{10} electronic configurations, are versatile for various applications due to their flexible coordination environments and ability to form highly ordered hierarchical structures. They show promise in electrocatalysis, energy storage, photovoltaics, and fuel cells. Literature reports have demonstrated their electroactive behaviors, such as low overpotentials for the HER and OER, and specific capacitances when used as electrode materials in supercapacitors.[18–22]

Continuing research efforts in this direction, we have developed a d^{10} metal-based COP, abbreviated as Zn(DAB), with 3,3′-diaminobenzidine (DAB) as the linker and evaluated its electrochemical performance as an electrode material for supercapacitors and as an electrocatalyst towards the water-splitting reaction. The selection of Zn as the central metal in the COP is driven by its fascinating electronic properties and potential to enhance effective charge storage. Herein, we discuss a facile synthesis and detailed characterization of the COP, followed by its potential application in supercapacitors and electrochemical water splitting. The intriguing results obtained for the HER and OER with Zn(DAB) further motivated us to investigate the electrocatalytic behavior of Cd(DAB), reported by us previously. The results obtained for Cd(DAB) as an electrocatalyst are also discussed later in the present manuscript.

Materials and methods

Materials

All the chemicals procured were utilized without modification. Analytical grade solvents obtained from Merck were dried using customary protocols before use. 3,3′-Diaminobenzidine (DAB) was obtained from TCI Chemicals, whereas polyvinylidene fluoride (PVDF), *N*-methyl-2-pyrrolidone (NMP), Nafion and zinc acetate dihydrate ($Zn(OAc)_2{\cdot}2H_2O$) were obtained from Sigma-Aldrich.

Preparation of coordination polymer Zn(DAB)

Zn(DAB) was prepared *via* a facile, modified technique under ambient conditions (Fig. 1).[23–25] An aqueous solution of

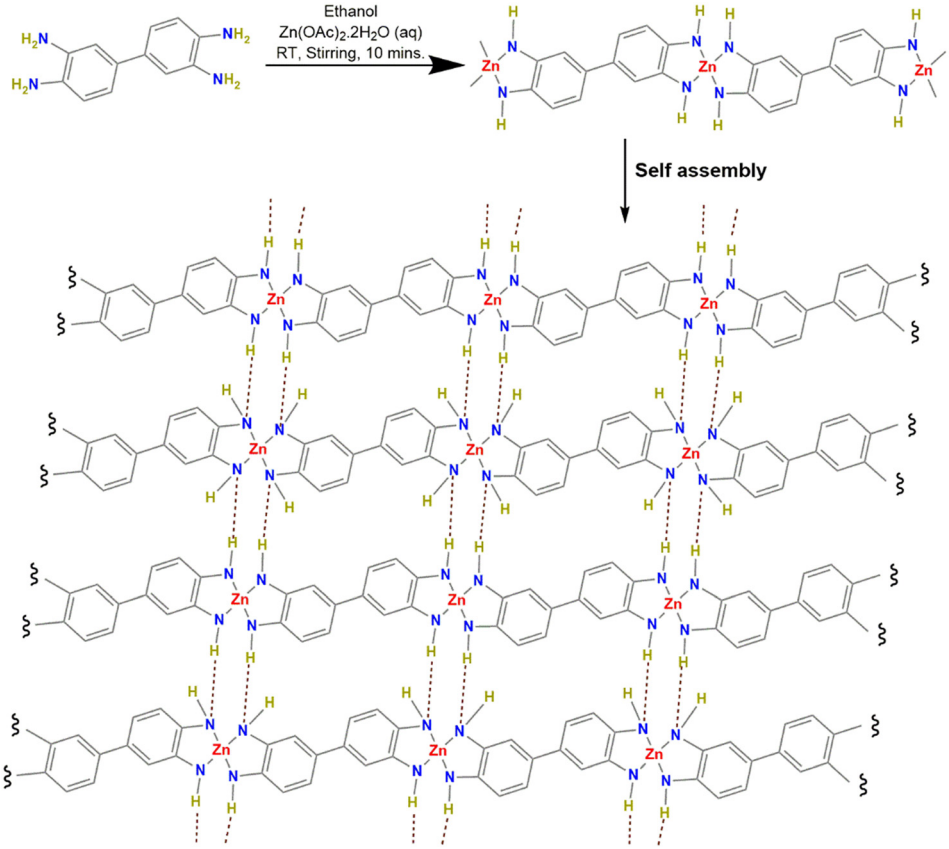

Fig. 1 Scheme for the synthesis of Zn(DAB).

metal acetate, $Zn(OAc)_2{\cdot}2H_2O$ (1.09 g, 5 mmol), was mixed with an ethanolic dispersion of DAB (1.074 g, 5 mmol) and stirred for 10 min at room temperature. The obtained precipitate was filtered and washed multiple times with water and ethanol, followed by heating in ethanol at 60 °C in a hot air oven for 12 h. The precipitate was centrifuged with multiple washings using water and ethanol. The COP was then obtained as a dark brown coloured crystalline powder.

Characterization of Zn(DAB)

Standard spectroscopic and electron microscopic characterization techniques were used to understand the nature, morphology, and composition of the prepared COP, Zn(DAB). A Rigaku Smart Lab X-ray diffractometer equipped with Cu Kα radiation was employed for X-ray diffraction (XRD) studies. The Raman spectroscopic data and FTIR spectra were obtained using a Raman spectroscope with 532 nm excitation (Horiba Jobin Yvon XploRA PLUS V1.2 MULTILINE) and a PerkinElmer Spectrum 1000 FT-IR spectrometer, respectively. X-ray phototelectron spectroscopy (XPS) was conducted with a PHOIBOS 100/150 delay line detector (DLD) with Al Kα (1486.6 eV) dual anode as the source with a power of 385 W and anode voltage of 13.85 kV. The sample current measured with a pico-ammeter was found to be 175.6 nA on the sample surface. The XPS was taken with a pass energy of 50 eV. As an internal reference for the absolute binding energy, the C-1s peak (284.5 eV) was used. The structural, morphological, and compositional analysis of the COP was carried out using field emission scanning electron microscopy (FESEM) with energy-dispersive spectra (EDS) and confirmed by high-resolution transmission electron microscopy (HRTEM) employing Carl Zeiss Supra 55 and Thermo Fisher Scientific Talos F200S G2 instruments, respectively. Additionally, the three-dimensional surface profile of the COP was obtained using a Zeta-20 KLA Tencor optical profilometer. Thermal stability was evaluated using thermogravimetric analysis (TGA) employing NETZSCH STA 2000 analyzer.

Electrochemical measurements

A CHI608E electrochemical workstation (CH Instruments Inc., USA) equipped with a three-electrode system was utilized for electrochemical measurements. Supercapacitance measurements were carried out with calomel electrode as reference electrode, Pt wire as counter electrode, and the prepared sample coated on Ni foam as working electrode using 3 M KOH as the electrolyte. The working electrode was prepared by drop casting an aqueous slurry of sample (1.5 g), activated carbon (0.289 g), 0.0938 g of polyvinylidene fluoride (PVDF), and 60 μL *N*-methyl-2-pyrrolidone (NMP) on Ni foam and drying it overnight. Cyclic voltammetry (CV),

galvanostatic charge–discharge (GCD), and electrochemical impedance spectroscopy (EIS) were the techniques used to evaluate the energy storage behaviour of the prepared sample at room temperature. The specific capacity (Cs), energy density (E) and power density (P) were obtained using eqn (1), (2), and (3), respectively.

$$\mathrm{Cs} = \frac{I \times \Delta t}{m \times V} \quad (1)$$

$$E = \frac{1}{2} \times \frac{\mathrm{Cs} \times V^2}{3.6} \quad (2)$$

$$P = \frac{E \times 3600}{\Delta t} \quad (3)$$

Water splitting studies were also conducted in an electrochemical cell with a three-electrode system with working electrode, reference electrode (calomel electrode), and counter electrodes (Pt wire) in 1 M KOH as the electrolyte. The working electrode was prepared by drop casting the catalyst ink comprising the COP (50 mg), Nafion (60 μL), ethanol (60 μL), and water (60 μL) on Ni foam and drying it overnight at 60 °C. Cyclic voltammetry (CV), linear sweep voltammetry (LSV), and electrochemical impedance spectroscopy (EIS) were used for the investigation. LSV was carried out at a scan rate of 5 mV s^{-1}, and overpotentials were obtained at a current density of 10 mA cm^{-2}. The potential (V *vs.* RHE) was calculated using eqn (4).

$$E(\mathrm{V}\ vs.\ \mathrm{RHE}) = E + (0.0591 \times \mathrm{pH}) + 0.241 \quad (4)$$

Results and discussion

Characterization of Zn(DAB)

The X-ray diffractogram of both ligand and COP is depicted in Fig. 2a. The peaks in the XRD pattern of DAB (Fig. 2a, black trace) observed at 2θ = 16.2°, 18.2°, 19.6°,

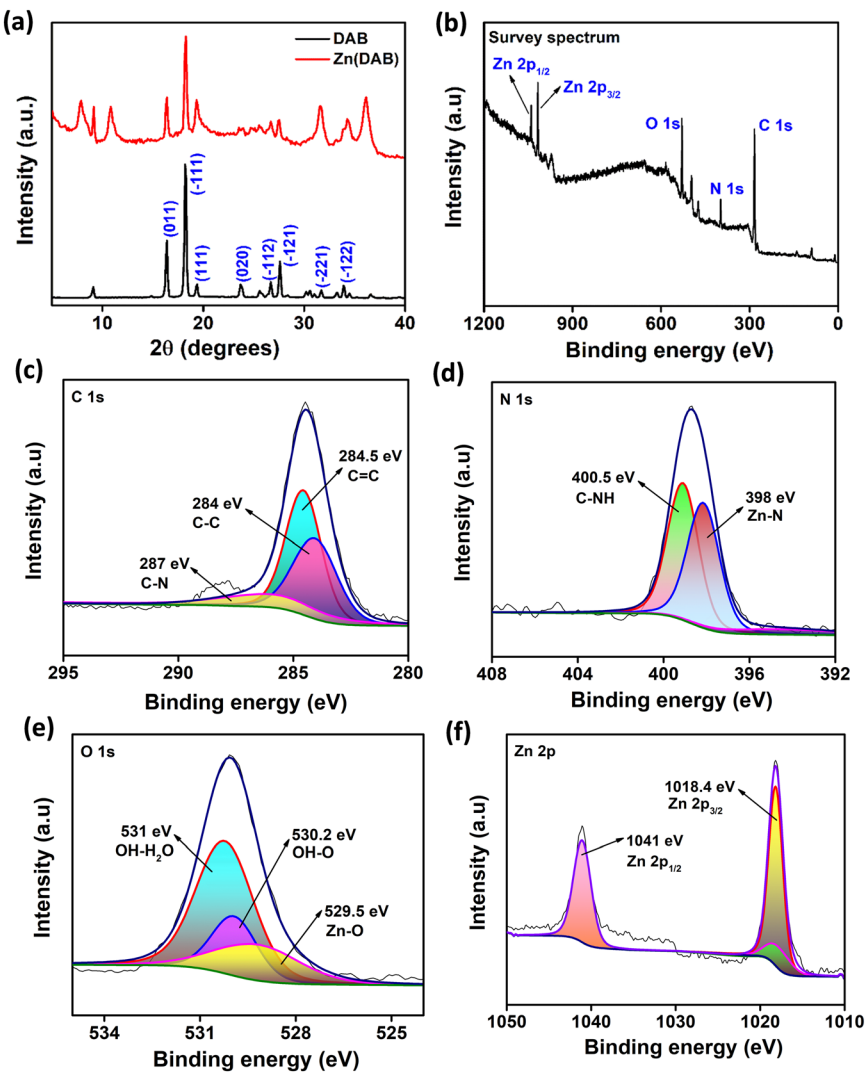

Fig. 2 (a) XRD plot of Zn(DAB). (b) XPS survey spectrum of Zn(DAB). High-resolution XPS spectrum indicating the (c) C 1s region, (d) N 1s region, (e) O 1s region, and (f) Zn 2p region.

23.8°, 26.7°, 27.8°, 31.6° and 33.9° correspond to (011), (−111), (111), (020), (−112), (−121), (−221) and (−122), respectively.[23] The reflections of all major planes of DAB are present in the profile of Zn(DAB), confirming its successful formation. Overall, the X-ray profile of the COP (Fig. 2a, red trace) shows a reduction in intensity as compared to that of DAB, which may be ascribed to its extended polymerized structure obtained as a result of self-assembly between infinitely long coordination strands. It exhibits distinct low-angle reflections between 5° and 15°, indicative of a periodic layered arrangement within the polymeric coordination framework. Such low-angle peaks are characteristic of layered materials and reflect ordered interlayer spacing arising from 2D stacked structures.[26,27] As observed, the (020) and (−122) planes appear to be shifted in Zn(DAB), in comparison to the X-ray pattern of DAB, pointing towards the presence of strain effects in the crystal lattice of the COP. Moreover, the absence of peaks at 32.5°, 36.3° and 47.1° (JCPDS card no 36-1451) in Zn(DAB) (Fig. S1†) eliminates the possibility of the presence of ZnO[28,29] or any unreacted precursor. Additionally, a few minor, unassigned peaks are observed in the pattern. These can be attributed to partially ordered domains or residual intermediates that may form during the coordination polymerization process. Such behavior is frequently reported in similar COPs, where broad, diffused, or minor reflections are associated with semi-crystalline or amorphous polymeric frameworks lacking long-range periodicity.[30] In the absence of single-crystal XRD data, precise indexing of these reflections remains a known limitation, common to polymeric coordination frameworks.

The chemical states and composition of the elements in the COP were analyzed using X-ray photoelectron spectroscopy (XPS). The resulting survey spectrum is displayed in Fig. 2b. Peaks detected at binding energies of 283.8 eV, 398.3 eV, 529.8 eV, 1017.8 eV, and 1040.8 eV correspond to the C 1s, N 1s, O 1s, Zn $2p_{3/2}$, and Zn $2p_{1/2}$ regions, respectively. Notably, the binding energies and assignments for the C 1s and N 1s peaks were consistent with those reported for DAB in the literature, confirming the retention of the ligand's core structure upon coordination.[31,32] Detailed insights into the elemental composition, chemical states, and bonding environments were obtained through high-resolution scans for each peak. The corresponding spectra for C 1s, N 1s, O 1s, and Zn 2p are presented in Fig. 2c–f, respectively. The C 1s spectrum displays peaks centered at 284 eV, 284.5 eV, and 287 eV. The combination of peaks at 284 eV and 284.5 eV corresponds to C–C and C═C, essentially due to the aromatic ring structure in the ligand, DAB. The peak at 287 eV corresponds to C–N bonding, also present in the ligand molecule.[33] The N 1s spectrum shows distinct peaks corresponding to different nitrogen environments in the sample. The peaks located at 400.5 eV are attributed to C–NH interactions, present in the DAB moiety, representing N in a sp^3 environment. Additionally, another peak present at 398 eV is indicative of Zn–N bonding, pointing towards the coordination of Zn(II) ions with N from DAB.[34] Moreover, the C 1s and N 1s peaks observed as well as the bonding characteristics seen were consistent with those reported for DAB-based COPs in our previous studies.[35,36]

The O 1s spectrum of Zn(DAB) exhibits peaks corresponding to adsorbed and surface-bound H_2O molecules. Peaks located at 530.2 eV and 531 eV are ascribed to OH–O and OH–H_2O interactions, respectively.[37] Another peak located at lower binding energies, 529.5 eV, reflects the presence of Zn–O, where oxygen is coordinated with Zn(II) in the Zn-based COP, completing the coordination environment of Zn(II) ions.[38]

The Zn 2p high-resolution spectrum typically exhibits two main peaks due to spin–orbit splitting, representing the Zn $2p_{3/2}$ and Zn $2p_{1/2}$ core levels. Peaks located at 1018.4 eV and 1041 eV are attributed to Zn $2p_{3/2}$ and Zn $2p_{1/2}$, respectively, indicating the chemical state of Zn(II) in the COP.[39–41]

The FTIR spectra of the ligand (black trace) and the COP (red trace) are shown in Fig. 3a. The fingerprint region (1500–400 cm^{-1}) of Zn(DAB) comprises a set of vibrations, which appear to be significantly different in comparison to DAB. The vibration band at 451 cm^{-1} corresponds to Zn–N stretching in Zn(DAB),[42] pointing towards the formation of a metal–ligand coordinate bond with N as the donor site. The peaks at ~1260 cm^{-1} and ~1620 cm^{-1} in the COP represent C–N and C–C stretching, respectively.[43] The sharp vibration peaks at 3350 cm^{-1} and 3395 cm^{-1} seen in DAB correspond to free amine stretching. The broadening of these peaks (3419 cm^{-1}) in Zn(DAB) suggests N-4 interaction as a result of coordination between metal ions and nitrogen from the ligand.[44] The Raman spectrum of Zn(DAB) shown in Fig. 3b (red trace) appears to be distinctly altered as compared to that of the ligand (Fig. 3b, black trace) and features two prominent bands at 1400 cm^{-1} and 1540 cm^{-1}. These bands resemble the D and G bands found in graphitic (2D) materials, which are typically observed at 1360 cm^{-1} and 1560 cm^{-1}, respectively. In graphitic materials, the G band is associated with C–C stretching, indicative of sp^2 carbons. The D band, on the other hand, is attributed to the breathing modes of sp^2 carbon atoms and is a double resonance band arising from a one-phonon lattice vibrational process.[45–47] These observations imply a 2D structure for the synthesized COP. This inference is further supported by FESEM and HRTEM images, which are discussed in later sections. Additionally, the presence of a broad band at 2889 cm^{-1} indicates multiple stacked layers within the COP.

The UV-Vis spectrum of the COP and the ligand are depicted in Fig. 3c with red and black traces, respectively. Two peaks appearing at 277 nm and 310 nm can be attributed to the $\pi \rightarrow \pi^*$ and $n \rightarrow \pi^*$ transitions. At the outset, the spectrum of Zn(DAB) is similar to that of DAB with a noteworthy bathochromic shift, *i.e.*, the peaks corresponding to $\pi \rightarrow \pi^*$ and $n \rightarrow \pi^*$ transitions are observed at 288 nm and 324 nm in the COP. The appreciable red shift seen is suggestive of extended π-conjugation in the Zn(DAB)

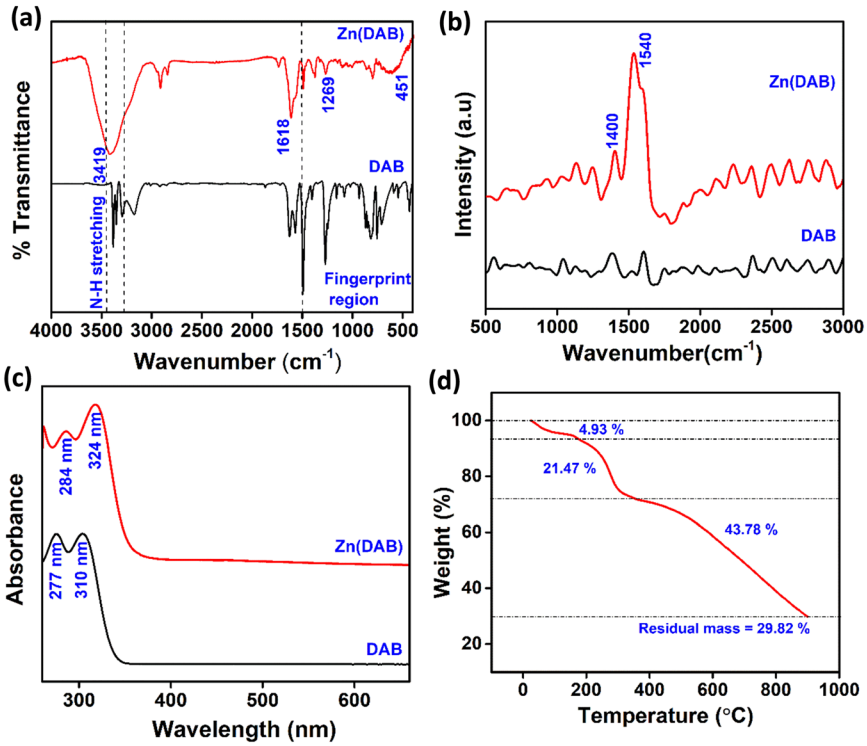

Fig. 3 (a) FTIR spectrum. (b) Raman spectrum. (c) UV-vis spectrum. (d) Thermogram of Zn(DAB).

on account of polymerization of infinitely long coordination strands. This can be attributed to an internal charge transfer between Zn^{2+} and DAB along with the hydrogen (H) bonds existing between 1D coordination strands.[48]

Thermogravimetric analysis (TGA) was conducted to understand the thermal stability of the as prepared COP, Zn(DAB). Fig. 3d showcases the thermogram of Zn(DAB). On subjecting it to high temperatures up to 800 °C, Zn(DAB) shows three major weight losses in the temperature regions, *viz.*, 100–200 °C (stage 1), 200–350 °C (stage 2) and 400–800 °C (stage 3). A slight loss in mass of 4.93% initially is ascribed to the loss of water molecules present as water of crystallization in the lattice of the COP. A further loss of 21.47% in stage 2 may be attributed to the partial breakdown of the polymeric framework due to the disruption of hydrogen bonds connecting the 1D strands. On heating it beyond 400 °C, Zn(DAB) undergoes further disintegration due to decomposition of DAB moieties, leaving a residual mass of 29.82%.[49]

Field emission scanning electron microscopy (FESEM) was conducted to obtain micrographs that reveal the surface morphology of the COP. The FESEM image of Zn(DAB) illustrates the two-dimensional layered structure of the COP, which is bundled on a large scale. The layers in Zn(DAB) have an average length of 1.155 μm with an interlayer spacing of 0.098 μm (Fig. 4a). Cd(DAB), synthesized by us previously,[25] was also assessed for its layer dimensions. It was found that the layers in the Cd-based COP are slightly longer (1.981 μm) and have a greater interlayer spacing of 0.187 μm (Fig. S2a†). These flat layers are stacked one above the other and are observed to form thick bundles. Longer 2D layers may result in improved mechanical properties along the plane of the layers. The extended and ordered arrangement can contribute to increased strength and stiffness in the material's specific direction. The increased length of planar sheets in Cd(DAB)

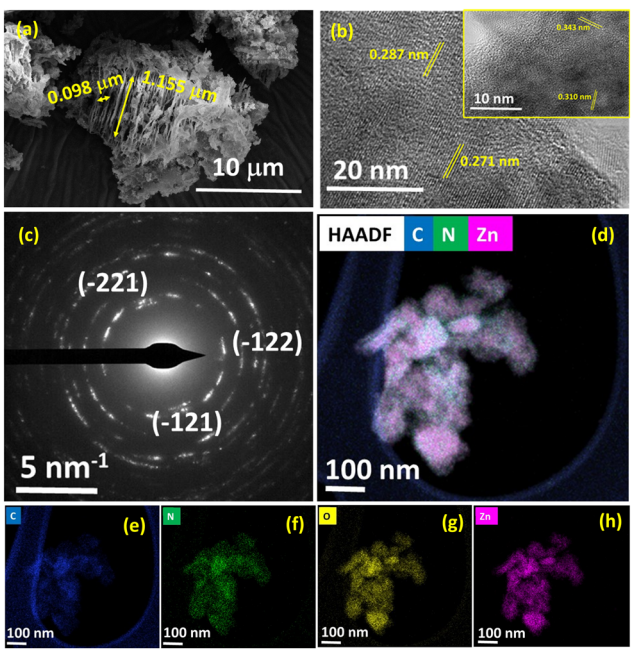

Fig. 4 (a) FESEM image, (b) HRTEM image, (c) SAED pattern, and (d) HAADF-STEM image of Zn(DAB). (e–h) Elemental mapping of C, N, O, and Zn.

can be correlated with its X-ray pattern, as discussed previously,[25] which reveals a greater extent of polymerization in the Cd-based COP. The arrangement of coordination units in longer 2D layers can influence electronic and optical properties. Extended conjugation along the layers has impacted the electronic structure and resulted in improved electronic behavior in Cd(DAB). Further, energy-dispersive X-ray spectroscopy (EDS) was employed to corroborate the elemental composition of Zn(DAB). The weight percentage (wt%) of elements, *viz.*, C, N, O, and Zn, could be obtained by this technique. The EDS spectrum (Fig. S2b and c†) confirms the presence of C, N, O, and Zn in 30.64, 16.13, 22.26, and 30.97 wt%, respectively. High-resolution transmission electron microscopy (HRTEM) together with selected-area electron diffraction (SAED) experiment was used to examine the crystallographic structure of the COPs. The HRTEM images substantiated the two-dimensional sheets seen in the FESEM micrographs. Fig. 4b showcases the planar morphology of Zn(DAB). In the HRTEM image, fringes correspond to the contrast variations resulting from the diffraction of electrons by crystal lattice planes within the sample. These fringes represent the spacing between atomic planes within the material. By calibrating the HRTEM image the distance between fringes in the HRTEM image can be measured. This fringe width obtained can thus be correlated with the spacing between adjacent crystal lattice planes, called the interplanar spacing or *d*-spacing. The *d*-spacing is obtained from the XRD pattern using the Bragg equation (eqn (5)), where n is the order of the diffraction peak (usually 1), λ is the wavelength of the incident radiation (0.154 nm), d is the interplanar spacing, and θ is the angle of incidence of the X-ray beam. Hence the measured fringe widths 0.287 nm, 0.271 nm, 0.343 nm, and 0.310 nm (Fig. 4b) correspond to the (−221), (−122), (−112), and (−121) planes in the X-ray pattern of Zn(DAB). The consistency in the *d*-spacing values obtained provides additional confirmation of the COP's crystalline structure and validates its formation.

$$2d \sin\theta = n\lambda \quad (5)$$

The SAED pattern of Zn(DAB) is depicted in Fig. 4c. The polycrystalline character of the COP was confirmed by the diffraction pattern obtained from SAED experiment. Similar to interpreting HRTEM fringe width, the distance of diffraction spots from the center in the SAED pattern can be used to calculate *d*-spacing and thus identify the crystallographic planes responsible for each diffraction spot. The calculated *d*-spacing values obtained from the SAED pattern can be compared with those obtained from XRD analysis. The SAED pattern in this case successfully correlates with d-spacing values for the (−121), (−122) and (−221) planes in Zn(DAB). This provides additional validation of the crystal structure and orientation in the case of the novel COP, Zn(DAB).

To map the elements in the COP, high-angle annular dark-field (HAADF) scanning transmission electron microscopy (STEM) imaging was used. The HAADF-STEM image is shown in Fig. 4d for the Zn-based COP, and the elemental mapping is shown in Fig. 4e–h. The mapping illustrates the distribution of elements C, N, O and Zn across the proposed layered 2D structure. The presence of O in Zn-DAB may be ascribed to the presence of H_2O as water of crystallization in order to satisfy the coordination environment of Zn(II).

Based on our experimental results and published literature, the neutral nature of the novel complex described in this study was predicted and confirmed.[35] Previous reports consistently demonstrate that related complexes exhibit neutrality, with C–N bonds displaying partial double-bond character, further corroborating our proposed structure.[50–54] It is also well documented that the formation of metal complexes in solution, particularly in aqueous media, involves notable thermodynamic changes. Initially, an enthalpic decrease facilitates the coordination of unstable metal ions with small ligands, such as solvent molecules, forming intermediate complexes. As the reaction progresses, these weakly bound ligands are displaced by larger, multidentate ligands, which typically results in a reduction in entropy owing to the release of smaller solvent molecules. However, in systems where coordination numbers remain partially unsatisfied, such as in lanthanide-based complexes, residual small ligands may persist within the coordination sphere. Interestingly, when multidentate ligands are introduced, the system can experience an overall increase in entropy, since the association of two species incurs a lower entropy penalty than the simultaneous interaction of multiple individual ligands. As a result, most coordination reactions proceed spontaneously, being driven by favorable enthalpic and/or entropic contributions.[55–58]

Supercapacitance measurements of Zn(DAB)

It is evident from the above discussion that Zn(DAB) prepared in this study is a layered 2D material formed by the self-assembly of one-dimensional strands composed of coordination complexes between metal nodes and organic ligands. The synergy of two distinctive attributes, *viz.*, two-dimensionality and coordination networks, develop several physicochemical characteristics, especially high conductivity and redox behavior. Owing to the extended π-conjugation across the polymeric network, it must be capable of demonstrating excellent redox behavior with multielectron transfer reactions. By virtue of these promising features, we evaluated the energy storage behavior and electrocatalytic ability of Zn(DAB) for water-splitting studies (HER and OER). The energy storage behavior of Zn(DAB) was studied in a conventional three-electrode cell configuration by cyclic voltammetry (CV), galvanostatic charge/discharge (GCD) experiments, and electrochemical impedance spectroscopy (EIS) investigations.

Fig. 5a and S3a† depict the cyclic voltammograms of Zn(DAB) recorded in the potential window 0–0.5 V, with scan rates varying from 100 mV s^{-1} to 10 mV s^{-1} and from 10 mV

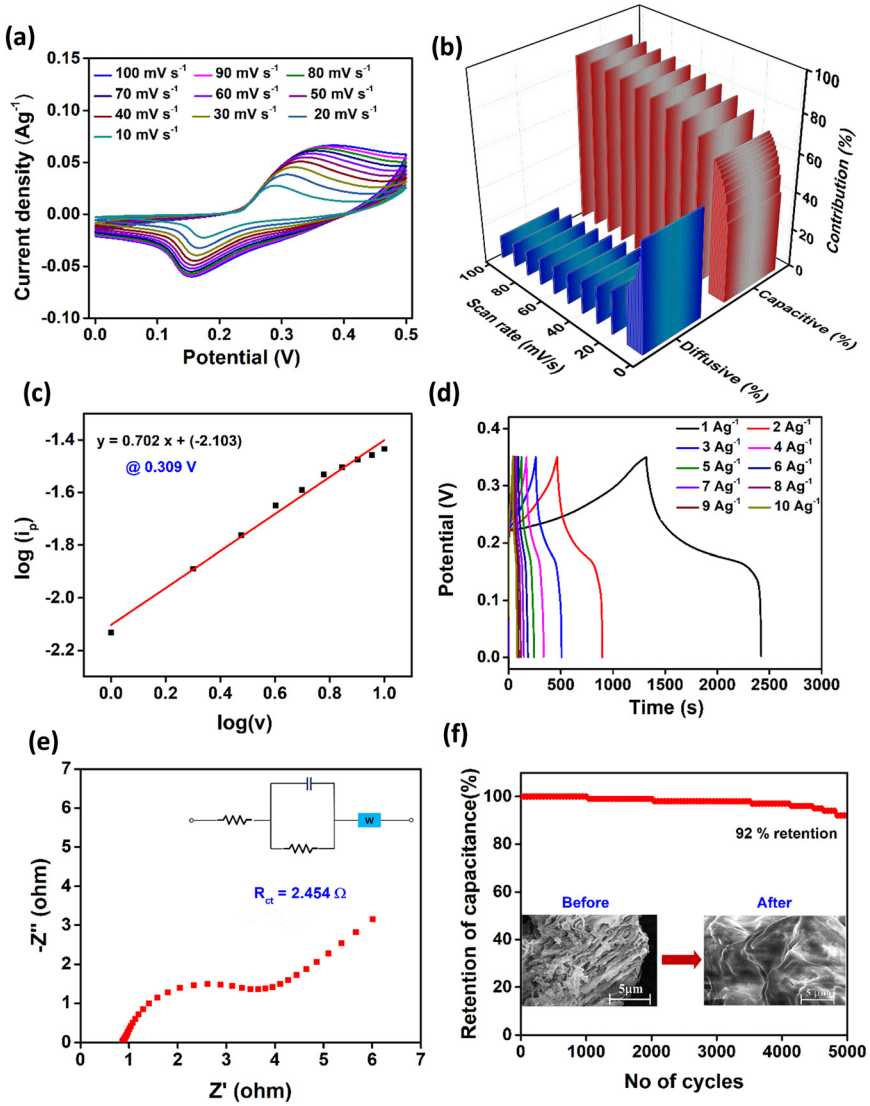

Fig. 5 (a) CV curves at different scan rates. (b) Bar representation of the surface current contributions at different scan rates. (c) Linear plot of log(i_p) *vs.* log *v*. (d) GCD curves at different current densities. (e) Nyquist plot. (f) Cyclic stability at 20 A g^{-1} of Zn(DAB).

s^{-1} to 1 mV s^{-1}, respectively. It is observed that with an increase in scan rate, an increase in current density occurs, thereby aggravating the CV curve area. This is attributed to the lowering in width of the diffusion layer in the electrolyte at higher scan rates. The cyclic voltammogram at 10 mV s^{-1} displays two peaks at 0.173 V and 0.287 V, corresponding to cathodic reduction and anodic oxidation, respectively. The CV curve of the working electrode in comparison with bare Ni foam (at 10 mV s^{-1}) provides evidence for the negligible contribution of Ni foam towards redox behavior (Fig. S3b†). For reference, a representative CV curve converted to the RHE scale is provided in the ESI† (Fig. S3c). The presence of two broad peaks in the CV curves represents specific redox reactions or capacitive contributions associated with the pseudocapacitive nature of the supercapacitor. In the present case, the pseudocapacitive nature of the material may essentially arise as a result of the layered morphology of the conducting COP, Zn(DAB).

Furthermore, a power law relationship (eqn (6)) was used to analyze the kinetic and diffusion-controlled contributions in the charge storage dynamics of the COPs. This involved examining the peak current (i_p) observed at a specific potential and scan rate (v in V s^{-1}) to differentiate between surface capacitive (k_1v) and diffusive ($k_2v^{1/2}$) contributions.

$$i_p = k_1v + k_2v^{1/2} \quad (6)$$

Fig. S3d† depicts a linear plot of $i_p/v^{1/2}$ *vs.* $v^{1/2}$ (at 0.309 V), where the slope and *y*-intercept values correspond to k_1 and k_2, respectively.[59] These values help further elucidate the capacitive (k_1v) and diffusive ($k_2v^{1/2}$) contributions at different scan rates. The current contributions at different scan rates are depicted in Fig. 5b. The capacitive contribution in Zn(DAB) increased from 42.1% (at 1 mV s^{-1}) to 87.9% (at 100 mV s^{-1}). The change in capacitive contribution with scan rate demonstrates the pseudocapacitive nature of the electrode

material. At low scan rates, Zn(DAB) possibly stores energy through a diffusion-limited process, where ions have sufficient time to penetrate the bulk of the active material layers. This results in more prominent redox peaks as the layered structure allows ion intercalation and deintercalation over longer time scales. As the scan rate increases, the capacitive process dominates due to the inability of ions to fully diffuse into the bulk of the material. This is reflected by a reduction in peak intensity and a shift in peak positions, indicating that the reaction is limited by ion diffusion. To further validate these conclusions, the *b*-value was obtained from a plot of $\log(i_p)$ *vs.* $\log(v)$ following eqn (7) (Fig. 5c).

$$i_p = av^b \tag{7}$$

In the present case, Zn(DAB) revealed an intermediate *b*-value of 0.702, indicating that the diffusion-controlled process dominates, but there is still a significant capacitive contribution.[60,61] Furthermore, Trasatti analysis was employed (eqn (8)) to quantitatively distinguish the capacitive and diffusion-controlled contributions to the total charge storage in Zn(DAB).

$$C = C_{\text{surface}} + \frac{C_{\text{diffusion}}}{v^{1/2}} \tag{8}$$

where C is the capacitance at a given scan rate (v), C_{surface} is the capacitive (surface-controlled) contribution, and $C_{\text{diffusion}}$ represents the diffusion-controlled contribution. A plot of C *versus* $1/v^{1/2}$ allows for the extrapolation of the linear graph to obtain C_{surface} at infinite scan rate ($1/v^{1/2} \rightarrow 0$) and C_{total} at zero scan rate ($1/v^{1/2} \rightarrow \infty$).[62] The analysis yielded a C_{surface} value of 0.05373 F g^{-1} and a C_{total} of 1.835 F g^{-1}, from which the $C_{\text{diffusion}}$ was determined to be 1.78127 F g^{-1} (Fig. S4a†). These results indicate that a major fraction of the charge storage arises from diffusion-controlled processes, with a noticeable but smaller capacitive contribution.

This suggests that the synthesized COP, Zn(DAB), exhibits diffusion-controlled behavior characterized by the reversible insertion and extraction of electrolyte ions into the material's interlayer spaces during the charge–discharge cycle. During the charging process, electrolyte ions may intercalate into the layers of the material. The layered structure may facilitate ion movement, but ion diffusion into the bulk of the material is slower, leading to a diffusion-controlled mechanism. This is consistent with the observed *b*-value of 0.702, indicating that the ion transport is not purely surface-confined but involves bulk diffusion as well. The intercalation process may induce a reversible change in the oxidation state of the active metal, Zn(II) ions, contributing to faradaic charge storage. Upon discharging, the electrolyte ions may de-intercalate from the interlayers and return to the electrolyte.[63,64] However, due to the diffusion-limited nature of the process, ion extraction is slower than in pure capacitive systems, though still faster than in battery-type materials. This mixed process, involving both near-surface faradaic reactions and bulk ion diffusion, is typical of pseudocapacitive behavior.

Galvanostatic charge–discharge (GCD) curves aid in understanding the charge–discharge time of the material and thus help in calculating the specific capacitance. The GCD curves obtained within the potential window 0–0.35 V at different current densities are shown in Fig. 5d. The shape of the curves is analogous to those obtained for pseudocapacitors. A higher discharge time is achieved at lower current densities. From the curve, the specific capacitance of Zn(DAB) at 1 A g^{-1} is calculated to be 2091.4 F g^{-1}. A plot of specific capacitance calculated at different current densities is depicted in Fig. S4b.† The plot shows the sharp decrease in specific capacitance with increasing current density owing to shorter discharge times. The energy density and power density of Zn(DAB) were calculated to be 35.58 Wh kg^{-1} and 116.67 W kg^{-1}, respectively. The outstanding specific capacitance obtained for Zn(DAB) can be correlated with its surface roughness. The average roughness (S_a) and root mean square roughness (S_q) for the realized COP were found to be 4.805 μm and 6.309 μm, respectively. The roughness of the electrode surface can influence the interface between the electrode and the electrolyte, thereby providing more active sites for the adsorption/desorption of ions, facilitating faster charge/discharge kinetics and improving energy storage performance. A rough surface may also provide a higher effective surface area and more pathways for the electrolyte to penetrate, leading to enhanced ion transport and improved electrochemical performances.[65] Fig. S5† shows the 2D and 3D view of Zn(DAB) obtained from Optical Profilometry.

A Nyquist plot obtained from electrochemical-impedance spectroscopy (EIS) measurements aids in finding the charge transfer resistance (R_{ct}) of the electrode material. A lower R_{ct} value serves as evidence for the highly conducting nature of the electrode material, which manifests into excellent energy storage behavior. From the Nyquist plot (Fig. 5e), the R_{ct} value of Zn(DAB) is estimated to be 2.454 Ω, indicating its semiconducting properties. The COP was also examined for its stability at a current density of 20 A g^{-1}. It is clear that Zn(DAB) shows 92% capacitive retention after a period of 5000 charge–discharge cycles (Fig. 5f). The FESEM images of the COP after 5000 charge–discharge cycles are shown in Fig. S6.† It is evident that Zn(DAB) did not undergo any decomposition or disintegration. However, a minor change in layered morphology due to possible restacking is observed.

Fabrication of asymmetrical supercapacitor device

An asymmetric supercapacitor device was assembled by using Zn(DAB) as the positive electrode and commercially available activated carbon as the negative electrode. To prepare the working electrode, 0.3 g of Zn(DAB) was thoroughly mixed with activated carbon and PVDF in a weight ratio of 8 : 1 : 1 using NMP as the solvent to form a homogeneous slurry. This slurry was uniformly coated onto a pre-cleaned nickel foam substrate and dried at 60 °C under vacuum for 12 h. The counter electrode was prepared by following a similar procedure using activated carbon. A 3 M KOH aqueous

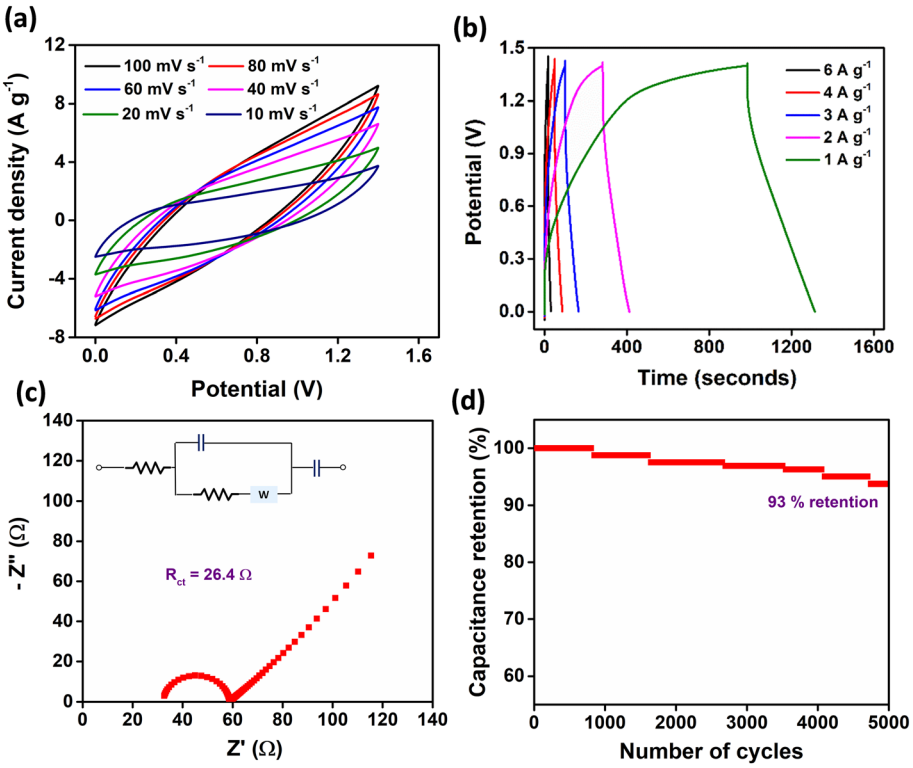

Fig. 6 (a) Cyclic voltammograms of Zn(DAB) at various scan rates, (b) GCD curves at different current densities, (c) Nyquist plot, and (d) cyclic stability of Zn(DAB) at a current density of 6 A g^{-1} using a two-electrode system.

solution was employed as the electrolyte, and a polypropylene membrane served as the separator. The assembled device was then evaluated using electrochemical techniques such as cyclic voltammetry (CV), galvanostatic charge–discharge (GCD), and electrochemical impedance spectroscopy (EIS).

The CV curves of the device, shown in Fig. 6a, were recorded within a potential window of 0–1.4 V at varying scan rates from 10 mV s^{-1} to 100 mV s^{-1}. The CV profiles exhibit a shape that is intermediate between the ideal rectangular form, characteristic of pure electric double-layer capacitance (EDLC), and pronounced, well-defined redox peaks indicative of strong faradaic reactions. The appearance of broad, hollow peaks and a degree of symmetry about the zero-current axis suggests the pseudocapacitive nature of the electrode material. This intermediate shape is attributed to the contribution of activated carbon, which is well known for displaying EDLC behavior, combined with the pseudocapacitive characteristics of Zn(DAB).

Further insights into the charge storage behavior are provided by the GCD curves, depicted in Fig. 6b. These curves, recorded within the same potential window of 0–1.4 V, show a predominantly triangular shape with slight deviations from perfect linearity, confirming the pseudocapacitive behavior of the Zn-based COP. The specific capacitance of the Zn(DAB) electrode in the two-electrode system was found to be 785.26 F g^{-1} at a current density of 1 A g^{-1}. In terms of energy and power performance, the device achieved an energy density of 213.7 Wh kg^{-1} and a power density of 2333.3 W kg^{-1}. EIS analysis (Fig. 6c) reveals a charge transfer resistance (R_{ct}) of 26.4 Ω, indicating moderate resistance. Fig. 6d demonstrates the device's excellent cycling stability, with 93% capacitance retention after 5000 charge–discharge cycles. Hence, the Zn(DAB) and activated carbon-based asymmetrical supercapacitor exhibits impressive electrochemical performance, combining high specific capacitance, good energy and power density, moderate resistance, and excellent stability.

Electrocatalytic water splitting

Electrocatalysis essentially requires catalysts with appropriate electronic structures to adsorb water molecules, facilitate electron transfer, and stabilize intermediate species formed during the reaction. In continuation with our previous works[23–25] and based on the discussion above, it is evident that d^{10} metal-based COPs demonstrate ionic diffusion and remarkable energy storage behavior. Hence, the layered COPs must be capable of facilitating water splitting electrochemically. This served as a motivation to further investigate the electrocatalytic ability of Zn(DAB) for water splitting studies, *viz.*, hydrogen evolution reaction (HER) and oxygen evolution reaction (OER). The notable results obtained for Zn(DAB) additionally inspired us to investigate the electrocatalytic behavior of Cd(DAB) reported previously. The synthesis and detailed structural investigation of Cd(DAB) has been discussed previously.[25] Hence, water splitting

measurements for the d^{10} metal-based COPs Zn(DAB) and Cd(DAB) were carried out in an electrolytic cell comprising a three-electrode cell configuration by cyclic voltammetry (CV), linear sweep voltammetry (LSV), Tafel plots and electrochemical impedance spectroscopy (EIS) investigations.

The LSV polarization curves for the HER obtained with Cd(DAB) (blue trace), Zn(DAB) (red trace), and Pt/C (green trace), recorded in the potential range 0.0 to −1.7 V, are depicted in Fig. 7a. For Pt/C (green trace), which is a well-known catalyst for the HER, the overpotential is relatively low (118 mV, here) compared to many other materials. The effectiveness of Pt/C as a catalyst is attributed to its excellent electrocatalytic properties and its ability to adsorb hydrogen atoms on its surface and facilitate their combination to form molecular hydrogen (H_2). However, the exact overpotential can depend on several factors, including the specific conditions of the experiment, the Pt loading on the carbon support, and the presence of any other catalytic or inhibiting species. It is seen that Cd(DAB) (blue trace) shows a marginally lower overpotential of 209 mV as compared to Zn(DAB) (red trace) with 263 mV at 10 mA cm^{-2}. Hence, the overpotential demonstrated by the newly synthesized COPs closely rivals that of Pt/C, showcasing their superior HER activity. Fig. S7a† shows the LSV curves of the COPs in comparison with bare Ni foam. The curves provide evidence for the negligible contribution of Ni foam to the electrocatalytic activity observed.

The mechanism followed by the HER in a specific material is anticipated with the help of Tafel slopes. The mechanism for HER in the basic medium involves the Volmer step (eqn (9)), followed by the Heyrovsky step (eqn (10)) or Tafel step (eqn (11)), with * as the active site. The Tafel slopes corresponding to these three steps are ~120, ~40, and ~30 mV dec^{-1}. A Tafel slope of 143.15 mV dec^{-1} and 145.7 mV dec^{-1} obtained for Zn(DAB) and Cd(DAB), respectively (Fig. 7b), is attributed to the Volmer–Heyrovsky mechanism followed by Volmer step as the rate-determining step.[66]

$$* + H_2O + e^- \rightarrow H^* + OH^- \quad (9)$$

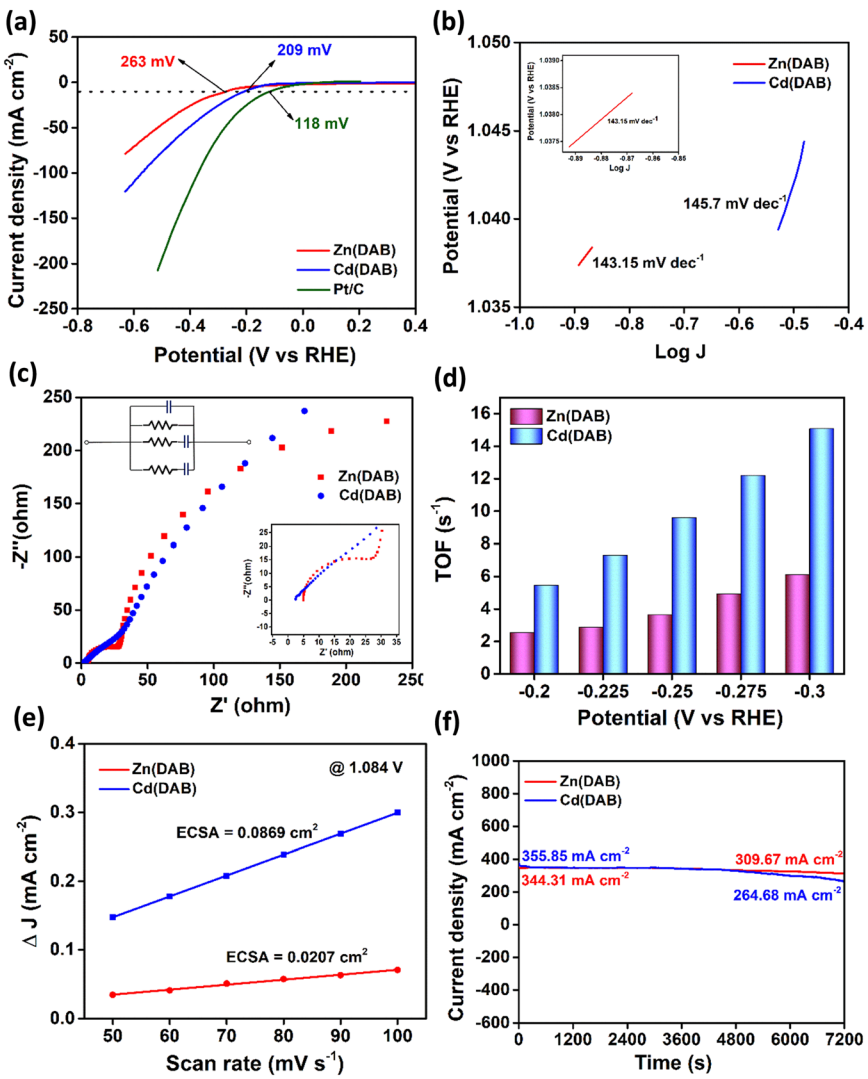

Fig. 7 (a) LSV curves, (b) Tafel plot, (c) Nyquist plot, (d) TOF for the HER. (e) Linear plot of current density *vs.* scan rate. (f) Stability test.

$$* + H_2O + e^- + H^* \rightarrow H_2 + OH^- + * \quad (10)$$

$$H^* + H^* \rightarrow H_2 + 2^* \quad (11)$$

Nyquist plot for HER is significant in determining the charge-transfer kinetics at the electrode–electrolyte surface. A material with lower charge transfer resistance (R_{ct}) demonstrates better electrocatalytic activity due to the smooth diffusion of ions in the electrolyte. Fig. 7c depicts the Nyquist plot for Zn(DAB) and Cd(DAB). The obtained R_{ct}, 22.625 Ω and 0.99 Ω, respectively, for Zn(DAB) and Cd(DAB) are in line with the higher overpotential of the former as compared to the latter. Turnover frequency (TOF) aids in assessing the number of active sites and the electrocatalytic activity of the material. TOF values are calculated in a wide potential window ranging from −0.3 V to 0.4 V. The TOF value attained for the HER by Cd(DAB) is 15 s^{-1}, which is nearly twice that achieved by Zn(DAB), 6.12 s^{-1} (Fig. 7d).

Non-faradaic CV curves were recorded in a small potential window, 0.0 to 0.03 V, with varying scan rates. The potential values obtained were converted to V *vs.* RHE using eqn (4). Fig. S7b and c† shows the cyclic voltammograms of Zn(DAB) and Cd(DAB). The anodic and cathodic branches of the CV curve are typically symmetrical, reflecting the reversible nature of capacitive charging and discharging processes. The curves obtained exhibit a rectangular shape, typically called non-faradaic CV curves, which is indicative of a purely capacitive response. The current response is proportional to the scan rate, and the shape is not affected by the presence of redox-active species. In the context of water splitting, non-faradaic voltammograms are recorded in a small potential window, typically when the electrochemical processes at the electrode–electrolyte interface do not involve significant redox reactions related to water splitting. This is useful for calculating double-layer capacitance and, hence, electrochemically active surface area (ECSA). From the non-faradaic rectangular curves, a linear plot of scan rate *vs.* current density is plotted (Fig. 7e), which is further used for the calculation of ECSA (eqn (12)). ECSA refers to the portion of a catalyst's surface that is directly involved in electrochemical reactions. The electrochemical double layer forms at the interface between the electrode and the electrolyte. The capacitance of this double layer (C_{dl}) is directly proportional to the ECSA. The ECSA can be calculated by measuring the capacitive current in response to potential changes. ECSA is given as the ratio of C_{dl} and C_s, where C_{dl} is the electrical double layer capacitance, and C_s is the specific capacitance of a smooth surface with an area of 1 cm^2. From previous reports, C_s for nickel foam is assumed to be 0.035 mF cm^{-2}.[67,68]

$$\text{ECSA} = \frac{C_{dl}}{C_s} \quad (12)$$

Zn(DAB) and Cd(DAB) demonstrated a C_{dl} of 0.000725 mF cm^{-2} and 0.00304 mF cm^{-2}, respectively. Hence, ECSA was calculated to be 0.0207 cm^2 for the former and 0.0869 cm^2 for the latter. Thus, the ECSA obtained is in line with the superior electrocatalytic activity exhibited by Cd(DAB) (lower overpotential for the HER), which can be associated with a greater number of active sites present in the COP.

The stability of the COPs was evaluated for a period of 2 h using bulk electrolysis (Fig. 7f). Zn(DAB) demonstrated slightly greater stability due to higher maintenance of current density. The current density in Zn(DAB) changed from 344.31 mA cm^{-2} to 309.67 mA cm^{-2}, whereas in Cd(DAB) the current density underwent a greater change from 355.85 mA cm^{-2} to 264.68 mA cm^{-2} over a period of 7200 s. As a representative case, the stability of Zn(DAB) was assessed over a continuous electrolysis period of 40 000 s (~11 h). During this prolonged operation, the current density gradually decreased, reaching 180 mA cm^{-2} (Fig. S7d†). This decline indicates a moderate loss in catalytic activity over time, suggesting partial deactivation of active sites or structural changes under sustained electrochemical conditions. The FESEM images of Zn(DAB) and Cd(DAB), obtained after stability test (for 2 h) are displayed in Fig. S8.† There is an evident lack of material disintegration or decomposition; nonetheless, a slight alteration in the layered morphology is noticeable, potentially indicating a degree of restacking.

From the mentioned results, it is clear that Zn(DAB) and Cd(DAB) exhibited remarkable HER activity in electrocatalytic water splitting studies. When tested for their affinity towards the OER, it was seen that the electrocatalytic activity was ordinary. Fig. S9a† depicts the LSV polarization curves for the OER. The overpotentials obtained for both the COPs were 409 mV and 437 mV, respectively, for Zn and Cd-based COP at 10 mA cm^{-2}. A marginally lower overpotential in the case of Zn(DAB) might be due to the decrease in kinetic energy barrier for the adsorption of the OER intermediates, generally observed for Zn-based materials.[69,70] The Nyquist plot for the OER is shown in Fig. S9b.† The charge-transfer resistance (R_{ct}) obtained for Zn(DAB) (0.585 Ω) was lower than that of Cd(DAB) (0.70 Ω), thereby corroborating its higher activity for the OER. The TOF values obtained, 11.47 s^{-1} and 9.61 s^{-1}, respectively, also substantiated the obtained results (Fig. S9c†). For the overall water-splitting reaction, Zn(DAB) gave a cell potential of 2.151 V, whereas Cd(DAB) demonstrated it to be 1.987 V (Fig. S9d†).

The performance variations between Zn(DAB) and Cd(DAB) stem from their electronic structures, bonding, and surface properties. Zn(DAB) exhibits higher surface area, enhancing active sites for charge storage and resulting in superior specific capacitance. Zn^{2+} centers, being relatively harder Lewis acids compared to Cd^{2+}, tend to stabilize oxygenated intermediates (such as OH*, O*, and OOH*) more effectively, thereby facilitating the multi-step oxidation pathway and resulting in a lower overpotential. Conversely, Cd(DAB) demonstrates better HER performance due to its larger ionic radius and softer Lewis acidity, resulting in a favorable electronic structure that may promote efficient hydrogen intermediate binding. These distinctions

underscore the role of surface characteristics and electronic interactions in their respective electrochemical behaviors.

Conclusion

A simplistic strategy has been employed to synthesize a d^{10} metal-based COP, Zn(DAB). The synthetic procedure developed is scalable and high-yielding. The COP was studied extensively for its composition and morphology utilizing standard spectroscopic and electron microscopic techniques. The XRD pattern illustrated the crystalline nature of the COP, whereas FESEM and HRTEM validated its multi-layered 2D planar structure. The electrochemical measurements of Zn(DAB) reveal its superior energy storage nature and electrocatalytic behavior for the HER. In particular, the COP exhibits a specific capacitance of 2091.4 F g^{-1} at 1 A g^{-1}, and stability of 92% capacitance retention after 5000 cycles at 20 A g^{-1}. Zn(DAB) and Cd(DAB) reveal significantly lower overpotentials for the HER, *viz.*, 263 mV and 209 mV, respectively, at a current density of 10 mA cm^{-2}. However, overpotentials obtained for the OER (409 mV and 437 mV, respectively) were slightly higher, owing to the inherent selectivity of the COPs for facilitating the HER. A lower overpotential observed in the case of Cd(DAB) for the HER is attributed to a greater diffusion of ions in its wider interlayer spaces. The COPs have shown remarkable stability over longer periods of time without appreciable change in current density. Hence, the COPs exhibit electroactive characteristics useful for energy storage *via* supercapacitors providing rapid charge–discharge and for energy generation through hydrogen production.

Data availability

The data supporting this article have been included as part of the ESI†

Author contributions

Samika Anand: data curation, conceptualization, methodology, investigation, writing – original draft. Abhishek Kumar: methodology, data curation, formal analysis. Kalathiparambil Rajendra Pai Sunajadevi: supervision, resources, conceptualization, project administration, writing – review and editing, validation. Channabasaveshwar V. Yelamaggad: conceptualization, resources, writing – review and editing, validation. Kaustava Bhattacharyya: data curation, formal analysis.

Conflicts of interest

The authors declare no competing financial interest.

Acknowledgements

The authors acknowledge the support of Christ University and the Centre for Nano and Soft Matter Sciences (CeNS). Samika Anand is grateful to the Department of Science and Technology, Government of India, for providing an INSPIRE fellowship.

References

1 T. M. Gür, *Energy Environ. Sci.*, 2018, **11**, 2696–2767.
2 I. Gunnarsdottir, B. Davidsdottir, E. Worrell and S. Sigurgeirsdottir, *Renewable Sustainable Energy Rev.*, 2021, **141**, 110770.
3 R. T. Yadlapalli, R. R. Alla, R. Kandipati and A. Kotapati, *J. Energy Storage*, 2022, **49**, 104194.
4 S. Wang, A. Lu and C. J. Zhong, *Nano Convergence*, 2021, **8**, 4.
5 D. Parra, L. Valverde, F. J. Pino and M. K. Patel, *Renewable Sustainable Energy Rev.*, 2019, **101**, 279–294.
6 P. D. Cavaliere, A. Perrone and A. Silvello, *Metals*, 2021, **11**, 1816.
7 K. Zhang and R. Zou, *Small*, 2021, **17**(37), 2100129.
8 X. Li, L. Zhao, J. Yu, X. Liu, X. Zhang and H. Liu, *Nano-Micro Lett.*, 2020, **12**, 1–29.
9 Y. Xu, K. Fan, Y. Zou, H. Fu, M. Dong, Y. Dou, Y. Wang, S. Chen, H. Yin, M. Al-Mamun, P. Liu and H. Zhao, *Nanoscale*, 2021, **13**, 20324–20353.
10 P. Chen, J. Ye, H. Wang, L. Ouyang and M. Zhu, *J. Alloys Compd.*, 2021, **883**, 160833.
11 W. Li, C. Wang and X. Lu, *Coord. Chem. Rev.*, 2022, **464**, 214555.
12 L.-Y. Guo, J.-F. Li, Z.-W. Lu, J. Zhang and C.-T. He, *ChemSusChem*, 2023, **16**(17), e202300214.
13 C. A. Downes and S. C. Marinescu, *ChemSusChem*, 2017, **10**, 4374–4392.
14 S. Abednatanzi, P. Gohari Derakhshandeh, H. Depauw, F.-X. Coudert, H. Vrielinck, P. Van Der Voort and K. Leus, *Chem. Soc. Rev.*, 2019, **48**, 2535–2565.
15 X.-H. Chang, Y. Zhao, M.-L. Han, L.-F. Ma and L.-Y. Wang, *CrystEngComm*, 2014, **16**, 6417–6424.
16 J.-Q. Liu, Z.-D. Luo, Y. Pan, A. Kumar Singh, M. Trivedi and A. Kumar, *Coord. Chem. Rev.*, 2020, **406**, 213145.
17 A. K. Ghosh, A. Hazra, A. Mondal and P. Banerjee, *Inorg. Chim. Acta*, 2019, **488**, 86–119.
18 A. Erxleben, *Coord. Chem. Rev.*, 2003, **246**, 203–228.
19 J. Chen, H. Zhang, B. Li, J. Yang, X. Li, T. Zhang, C. He, C. Duan and L. Wang, *ACS Appl. Energy Mater.*, 2020, **3**, 10515–10524.
20 D. Zhao, J. Song, X. Zhang, F. Wang, B. Li, L. Yang, Y. Deng, Q. Li and L. Fan, *CrystEngComm*, 2021, **23**, 6245–6252.
21 X. Sun, Y. Qu, G. Wang, T. Chen and G. Wang, *ChemistrySelect*, 2022, **7**(6), e202103660.
22 C. A. Downes and S. C. Marinescu, *Dalton Trans.*, 2016, **45**, 19311–19321.
23 S. Rahaman, M. B. Kanakala, M. Waldiya, A. Sadhanala, C. V. Yelamaggad and K. Pandey, *J. Power Sources*, 2023, **564**, 232801.
24 S. A. Bhat, N. B. Palakurthy, N. Kambhala, A. Subramanian, D. S. Shankar Rao, S. Krishna Prasad and C. V. Yelamaggad, *ACS Appl. Polym. Mater.*, 2020, **2**, 1543–1552.

25 S. Anand, S. D. K. R. Pai, A. Kumar and C. V. Yelamaggad, *ACS Omega*, 2024, **9**, 41807–41818.
26 H. Vanderstraeten, D. Neerinck, K. Temst, Y. Bruynseraede, E. E. Fullerton and I. K. Schuller, *J. Appl. Crystallogr.*, 1991, **24**, 571–575.
27 A. Leonardi and D. L. Bish, *Inorg. Chem.*, 2020, **59**, 5357–5367.
28 D. Pinheiro, A. Jose, N. Rajiv Bharadwaj, U. C. Jadan Resnik Jaleel and S. K. R. Devi, *ECS J. Solid State Sci. Technol.*, 2021, **10**, 071004.
29 A. Khorsand Zak, R. Razali, W. H. Abd Majid and M. Darroudi, *Int. J. Nanomed.*, 2011, **6**, 1399.
30 A. F. Sapnik, C. Sun, J. E. M. Laulainen, D. N. Johnstone, R. Brydson, T. Johnson, P. A. Midgley, T. D. Bennett and S. M. Collins, *Commun. Chem.*, 2023, **6**, 92.
31 Y. Zhao, J. Liu, N. Wang, Q. Li and M. Hu, *J. Mater. Chem. A*, 2018, **6**, 7566–7572.
32 Y. Lei, G. Lan, D. Zhu, R. Wang, X. Zhou and G. Li, *Appl. Organomet. Chem.*, 2018, **32**(8), e4421.
33 Y. Wang, X. Yang, J. Lou, Y. Huang, J. Peng, Y. Li and Y. Liu, *Molecules*, 2022, **27**, 8476.
34 C. Xie, L. Lin, L. Huang, Z. Wang, Z. Jiang, Z. Zhang and B. Han, *Nat. Commun.*, 2021, **12**, 4823.
35 S. A. Bhat, N. B. Palakurthy, N. Kambhala, A. Subramanian, D. S. Shankar Rao, S. Krishna Prasad and C. V. Yelamaggad, *ACS Appl. Polym. Mater.*, 2020, **2**, 1543–1552.
36 S. Rahaman, M. B. Kanakala, M. Waldiya, A. Sadhanala, C. V. Yelamaggad and K. Pandey, *J. Power Sources*, 2023, **564**, 232801.
37 S. Jain, J. Shah, N. S. Negi, C. Sharma and R. K. Kotnala, *Int. J. Energy Res.*, 2019, **43**, 4743–4755.
38 H. S. Casalongue, S. Kaya, V. Viswanathan, D. J. Miller, D. Friebel, H. A. Hansen, J. K. Nørskov, A. Nilsson and H. Ogasawara, *Nat. Commun.*, 2013, **4**, 2817.
39 D.-M. Feng, Y. Sun, Z.-Y. Yuan, Y. Fu, B. Jia, H. Li and T. Ma, *Mater. Renew. Sustain. Energy*, 2021, **10**, 8.
40 H. Zhang, W. Li, G. Qin, L. Fang, H. Ruan, M. Tan, F. Wu and C. Kong, *Appl. Phys. A: Mater. Sci. Process.*, 2018, **124**, 147.
41 R. G. Nair, S. Mazumdar, B. Modak, R. Bapat, P. Ayyub and K. Bhattacharyya, *J. Photochem. Photobiol., A*, 2017, **345**, 36–53.
42 B. Naureen, G. A. Miana, K. Shahid, M. Asghar, S. Tanveer and A. Sarwar, *J. Mol. Struct.*, 2021, **1231**, 129946.
43 M. Karabacak, S. Bilgili and A. Atac, *Spectrochim. Acta, Part A*, 2015, **150**, 83–93.
44 J. K. Cooper, A. M. Franco, S. Gul, C. Corrado and J. Z. Zhang, *Langmuir*, 2011, **27**, 8486–8493.
45 C. Wu, L. Dong, J. Huang and P. T. Williams, *RSC Adv.*, 2013, **3**, 19239.
46 H. Liu, T. Kuila, N. H. Kim, B.-C. Ku and J. H. Lee, *J. Mater. Chem. A*, 2013, **1**, 3739.
47 I. Childres, L. A. Jaureguib, W. Parkb, H. Caoa and Y. P. Chena, in *New Developments in Photon and Materials Research*, 2013, pp. 1–20.
48 L. Yang, Y. Yu, J. Feng, J. Wu, L. Jiang, Y. Dan and Y. Qiu, *J. Photochem. Photobiol., A*, 2018, **350**, 103–110.
49 Y. Wang, Y. Song, L. Zhao, N. Rahoui, B. Jiang and Y. Huang, *Polymers*, 2016, **8**, 420.
50 C. Alex, S. A. Bhat, N. S. John and C. V. Yelamaggad, *ACS Appl. Energy Mater.*, 2019, **2**, 8098–8106.
51 G. S. Hall and R. H. Soderberg, *Inorg. Chem.*, 1968, **7**, 2300–2303.
52 I. E. Maxwell and M. F. Bailey, *J. Chem. Soc., Dalton Trans.*, 1972, 935.
53 G. Ricciardi, A. Rosa, G. Morelli and F. Lelj, *Polyhedron*, 1991, **10**, 955–961.
54 H. Masui, A. B. P. Lever and E. S. Dodsworth, *Inorg. Chem.*, 1993, **32**, 258–267.
55 J. S. Dugdale, *Entropy And Its Physical Meaning*, Taylor & Francis, 2018.
56 J. M. Andrić, G. V. Janjić, D. B. Ninković and S. D. Zarić, *Phys. Chem. Chem. Phys.*, 2012, **14**, 10896.
57 C. Li and J. Zuo, *Adv. Mater.*, 2020, **32**(27), 1903762.
58 P. Perrot, *A to Z of Thermodynamics*, Oxford University Press on Demand, 1998.
59 T. Schoetz, L. W. Gordon, S. Ivanov, A. Bund, D. Mandler and R. J. Messinger, *Electrochim. Acta*, 2022, **412**, 140072.
60 Y. Liu, S. P. Jiang and Z. Shao, *Mater. Today Adv.*, 2020, **7**, 100072.
61 Y. Ge, X. Xie, J. Roscher, R. Holze and Q. Qu, *J. Solid State Electrochem.*, 2020, **24**, 3215–3230.
62 A. Nashim, S. Pany and K. M. Parida, *J. Energy Storage*, 2021, **42**, 103145.
63 R. Kumar and M. Bag, *J. Phys. Chem. C*, 2021, **125**, 16946–16954.
64 O. A. González-Meza, E. R. Larios-Durán, A. Gutiérrez-Becerra, N. Casillas, J. I. Escalante and M. Bárcena-Soto, *J. Solid State Electrochem.*, 2019, **23**, 3123–3133.
65 J. Wei, Y. Li, D. Dai, F. Zhang, H. Zou, X. Yang, Y. Ji, B. Li and X. Wei, *ACS Appl. Mater. Interfaces*, 2020, **12**, 5786–5792.
66 F. Bao, E. Kemppainen, I. Dorbandt, R. Bors, F. Xi, R. Schlatmann, R. van de Krol and S. Calnan, *ChemElectroChem*, 2021, **8**, 195–208.
67 C. C. L. McCrory, S. Jung, J. C. Peters and T. F. Jaramillo, *J. Am. Chem. Soc.*, 2013, **135**, 16977–16987.
68 Y. Xue, B. Huang, Y. Yi, Y. Guo, Z. Zuo, Y. Li, Z. Jia, H. Liu and Y. Li, *Nat. Commun.*, 2018, **9**, 1460.
69 K. Zhang, G. Zhang, J. Qu and H. Liu, *Small*, 2020, **16**(11), 1907001.
70 M. Huo, Z. Yang, C. Yang, Z. Gao, J. Qi, Z. Liang, K. Liu, H. Chen, H. Zheng and R. Cao, *ChemCatChem*, 2019, **11**, 1480–1486.